Available online at www.sciencedirect.com
SCIENCE DIRECT
International Journal of Heat and Fluid Flow 27 (2006) 684–695
International Journal of HEAT AND FLUID FLOW
www.elsevier.com/locate/ijhff

A computational study of the near-field generation and decay of wingtip vortices

T.J. Craft, A.V. Gerasimov, B.E. Launder *, C.M.E. Robinson

School of Mechanical, Aerospace and Civil Engineering, The University of Manchester, P.O. Box 88, Manchester M60 1QD, UK

Available online 5 April 2006

Abstract

The numerical prediction of the downstream trailing vortex shed from an aircraft wingtip is a particularly challenging CFD task because, besides predicting the development of the strong vortex itself, one needs to compute accurately the flow over the wing to resolve the boundary layer roll-up and shedding which provide the initial conditions for the free vortex.

Computations are here reported of the flow over a NACA 0012 half-wing with rounded wing tip and the near-field wake as measured by [Chow, J.S., Zilliac, G., Bradshaw, P., 1997. Turbulence measurements in the near-field of a wingtip vortex. NASA Tech Mem 110418, NASA.]. The aim is to assess the performance of two turbulence models which, in principle, might be seen as capable of resolving both the three dimensional boundary layer on the wing and the generation and near-field decay of the strongly accelerated vortex that develops from the wingtip. Results using linear and non-linear eddy-viscosity models are presented, but these both exhibit a far too rapid decay of the vortex core. Only a stress-transport (or second-moment) model that satisfies the "two-component limit", [Lumley, J.L., 1978. Computational modelling of turbulent flows. Adv. Appl. Mech. 18, 123–176.], reproduces the principal features found in the experimental measurements.
© 2006 Elsevier Inc. All rights reserved.

Keywords: Trailing vortex; Wing aerodynamics; CFD; Turbulence models; Second moment closure

1. Introduction

The serious impact of the trailing vortices from large aircraft is well known. Many examples exist of the damage caused to following aircraft caught up in the swirling wake shed from an upstream craft. While, at a practical level, guidelines exist for safe distances between aircraft, the issue of satisfactorily predicting the vortex formation and decay with CFD methods is far from being satisfactorily resolved. This is particularly relevant at the present time as there are considerable efforts underway to develop novel wing-tip devices to improve the aerodynamic performance of wings. Thus attention needs to be given to what impact such devices may also have on the trailing vortex and its decay characteristics to explore whether they can be designed to promote a more rapid dispersal of the vortex, a matter first raised by Carlin et al. (1989) and (as reported by Chow, 1994) Heffernan (1985).

As early as the mid-60s Batchelor (1964) had pointed out that, for a translating "line vortex", Bernoulli's equation and radial equilibrium requirements meant that, as the vortex rolled up, the pressure on the axis progressively fell, leading to an increase in the axial velocity above that in the free stream as one moved radially inwards to the vortex centre. This feature, it will be seen, is one of the principal characteristics to capture in modelling the near-field vortex. Later attempts to improve on Batchelor's simple arguments led to significantly different results (e.g. Moore and Saffman, 1973) which were not however in agreement with the bulk of experimental data. In fact, experimental studies from the period focused mainly on the medium field and in any event suffered from the difficulties of measuring a strongly swirling flow accurately with total pressure and hot-wire probes, e.g. Chigier and Corsiglia (1971, 1972), Lee and Schetz (1985). The studies showed, however, the

* Corresponding author. Tel.: +44 161 200 3701; fax: +44 161 200 3723.
E-mail address: brian.launder@manchester.ac.uk (B.E. Launder).

0142-727X/$ - see front matter © 2006 Elsevier Inc. All rights reserved.
doi:10.1016/j.ijheatfluidflow.2006.02.024

great importance of wing aspect ratio and angle of attack (and the chord Reynolds number, at least for low Re_c) on the character of the wing-tip vortex.

More recently Green (1991) and Green and Acosta (1991) used double-pulsed holography to measure the vortex development over the first ten chord lengths downstream from a NACA 66-209 rounded tip rectangular wing. Two chord lengths downstream from the tip they noted that, for a 10° angle of attack, the axial velocity in the vortex core reached a maximum value 60% greater than that in the free stream. Finally, we note the joint Stanford-NASA Ames study of the near-field vortex roll-up that will provide the focus for the present contribution, Chow (1994), Chow et al. (1997). These workers examined in unprecedented detail the flow over and immediately downstream of a NACA 0012 wing section with rounded tip and width equal to $0.75c$ at a single (10°) angle of attack using hot-wire and 7-hole probes. The rationale for their research was to provide a searching test for modern CFD methods and turbulence models. For that reason they considered only a single configuration and adopted the largest size of model consistent with avoiding severe tunnel interference (such as separation on the wind-tunnel walls). For a CFD comparison, this arrangement is convenient as the grid then naturally extends over the whole tunnel cross-section.

In fact, from the CFD standpoint, there are several challenges to modelling the trailing-vortex flow's development. The flow over the outboard part of the wing develops into a highly skewed, three-dimensional boundary layer that, as it detaches, rolls up to form the strong, nearly-axisymmetric trailing vortex. Thus, the whole wing boundary layer (on both the pressure and suction surfaces) has to be computed accurately to provide the initial conditions for the vortex computation itself. Likewise, the model of turbulence adopted also has to be capable of resolving accurately the complex wing boundary layer as well as the swirling free shear flow downstream.

It is thus, perhaps, not surprising that there have been relatively few CFD studies reported of the trailing vortex development from a conventional (as opposed to a delta) wing form. Srinivasan et al. (1988) used a thin-layer analysis to compute the flow over a helicopter blade-tip with the Baldwin–Lomax model of turbulence which showed poor agreement of the flow in the wake. De Jong et al. (1988) used a similar forward marching approach to compute the flow around and downstream from a NACA 0012 airfoil at approximately 6° and 11° angles of attack. Again, many key features of the vortex wake were wrongly predicted, for example the formation of an axial velocity excess was entirely missed. More recently, in conjunction with their experimental studies, the Stanford-NASA group have reported fully 3D (i.e. fully elliptic) computations of their flow, Dacles-Mariani et al. (1995), employing some 1.5×10^6 grid nodes. The basic model of turbulence used was the Baldwin and Barth (1990) one-equation eddy-viscosity model, though a number of ad hoc variants were explored to ascertain whether any gave better agreement with the measurements.

Although the scale of the computational task tends to encourage the use of such simple, abidingly stable, models of turbulence, the experimental data of swirling flows has shown that the phenomena cannot be captured at this level. Within the perspective of RANS-based turbulence modelling, the trailing vortex is an example of a flow with strong streamline curvature, a flow feature that is widely known to be inadequately represented by any linear eddy-viscosity model. Many attempts have been made to escape from the inherent weakness of a Boussinesq-viscosity stress–strain law by adding curvature-related source or sink terms to the empirical length-scale-determining equation. It is now generally accepted, however, that any widely valid approach needs to be focused on adopting a better model for the stress–strain rate connection itself, whether by way of a second-moment closure (solving transport equations for the Reynolds-stress components) or with a non-linear eddy-viscosity model (also known as an explicit algebraic stress model, Gatski and Rumsey, 2002). Even progression to such relatively advanced models by no means assures reliable predictions in all cases. For example, the early study by Launder and Morse (1979) of an axisymmetric swirling jet with a (still widely used) second-moment closure computed seriously wrong rates of spread which were traced to the model of the pressure–strain correlation in the stress-transport equations. It is noted, too, that the same model, if applied to flows near walls, requires near-wall corrections (tuned by reference to flows near an infinite plane wall) which can, by no means, be expected to cope with the conditions at the edge of a wing where the surface itself is strong curved. Finally,we note that all models from that period fail to predict the far-field characteristics of wakes unless the coefficients are specifically tuned for such flows. This is a serious handicap in handling the present class of flows which intrinsically involve a near-field and a far-field wake.

The present contribution reports a new computational study of the experiment of Chow et al. (1997). Although a linear eddy-viscosity model is used as a reference, the paper principally considers the performance of two models which, in principle, may be expected to be able to handle both the wing region and the wake region without modification to the model. The non-linear eddy-viscosity model of Suga (1995), (see also Craft et al., 1996b) has been successfully applied to both two- and three-dimensional flows around bends and to axially swirling flow in a pipe. The other model, the two-component-limit (TCL) second-moment closure, based on an idea of Lumley (1978) and developed at UMIST by a succession of doctoral workers has the merit of being able to handle flows near walls without explicit wall-proximity corrections (Launder and Li, 1994). It has also been applied successfully to a 3D bend flow (Iacovides et al., 1996) and has been shown to give far better agreement with experiment over a basket of free shear flows (albeit without swirl) than the

usual second-moment closure (Craft et al., 1996a). We note also that Sotiropoulos and Patel (1995) applied a predecessor version of the present TCL model (Launder and Shima, 1989) to the related problem of computing the boundary layer and downstream swirling near-wake for a model ship's hull. Close agreement with the experimental data was reported, superior to that returned by any of the other models considered. Finally, we note that the conference paper from which this present contribution has been developed has considered a more extensive range of models, albeit in less detail, Craft et al. (2005). Where appropriate, brief reference will be made to results reported in that work.

Section 2 below considers, in separate sub-sections, the modelling of the turbulent stress field and the numerical strategy adopted in gridding, in prescribing appropriate boundary conditions and in solving the system of transport equations. Thereafter, Section 3 examines the performance of the different models in simulating the observed behaviour. While, as noted, computations began upstream of the wing and the detailed boundary layers on the wing have had to be resolved in detail, because the detailed experimental data were focused on the downstream vortex behaviour, our attention here is likewise on this free-shear-flow jet/wake vortex region. We have, however, attempted to distinguish model weaknesses associated with computing the wing boundary layer from those associated with modelling the subsequent trailing vortex.

2. Numerical and physical models

2.1. Turbulence models

The main interest has been in seeing whether the complexities in the flow considered could be resolved with either of the turbulence models developed specifically to overcome inadequacies both of eddy-viscosity and conventional second-moment closures. The TCL model (see Appendix) documented in Craft and Launder (2001) and Launder and Li (1994) has been in use for well over a decade and been found capable of handling a diversity of complex strain fields. For present purposes its two most important features are a model of mean-strain effects on the pressure–strain process fully consistent with the two-component limit (that is, when the turbulent fluctuations lie in a plane) and a sink term in the dissipation rate (ε) equation dependent on the invariants of the Reynolds stress tensor. The second of these features allows the model to cope with both strong and weak free shear flows (including relatively good predictions of the axisymmetric free jet in stagnant surroundings and the far-field asymptotic wake) while the first enables it to compute complex flows near walls without the need to make reference to distance of a point from a rigid boundary, an especial advantage in handling bodies of complex shape. A simpler route has also been tried, the non-linear eddy-viscosity model (NLEVM) of Suga (1995) (see Craft et al., 1996b), whose details are also given in the Appendices. This was the first NLEVM to include cubic terms in the stress/deformation-rate constitutive equation, an elaboration essential to capture (approximately) the strong effects of streamline curvature on turbulence. The extra model coefficients thus introduced were fixed by considering a wide range of test flows including two wall flows with streamline curvature.

Except as noted below, wall boundary conditions have been applied by way of analytic wall functions (Craft et al., 2002) to avoid the excessively fine mesh needed to resolve the viscous sublayer itself. While these have been widely validated in non-equilibrium wall flows, they do not permit the strong velocity skewing across the sublayer that occurs in gas-turbine blading. However, for the present test-case, comparative tests of the TCL model with wall functions and with a model providing a 'low-Reynolds-number' treatment across the sublayer (the 1-equation scheme of Wolfshtein, 1969) showed little change in flow direction across this sublayer (as also implied by the sur-

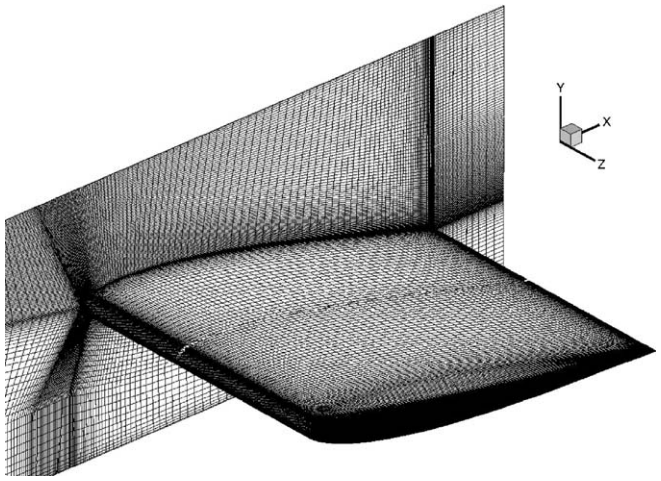

Fig. 1. Wing and wing-root wall surface grids.

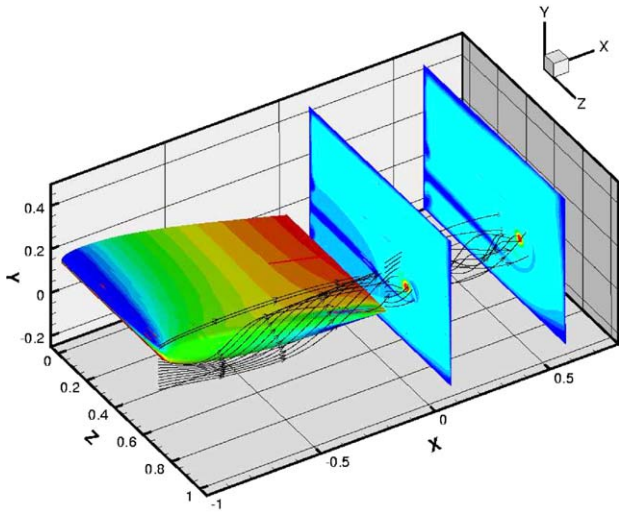

Fig. 2. Computed streamlines and pressure contours using the TCL model.

face streak-lines of Chow, 1994). Thus, the wingtip vortex, because it originates from the migration of air from the underside of the wing (unlike the situation in a gas-turbine stage) does not lead to velocity skewing within the near-wall sublayer. This fact enabled us to avoid the extra near-wall nodes required to resolve this semi-viscous layer while still being able to use a fine resolution away from the wing yet still keep the total storage demands within availability. The refinement of employing a more complex near-wall modelling was therefore not extended to other models and runs.

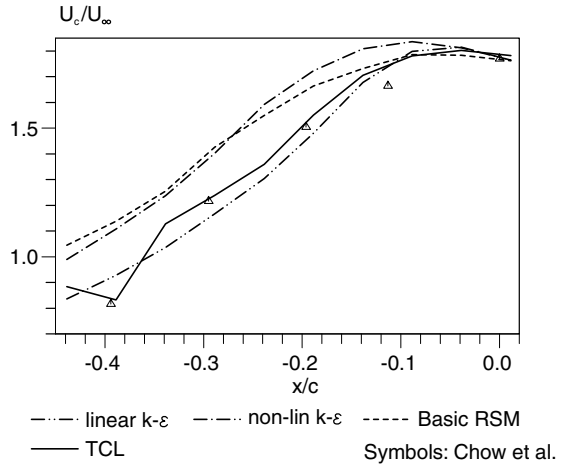

Fig. 3. Development of vortex-core axial velocity over the wing.

2.2. The test case, the numerical solver and the grid adopted

As noted above, the experimental test case examined is the flow over the NACA 0012 half-wing with rounded wing tip examined by Chow et al. (1997). The airfoil is set at a 10° angle of attack and installed in a wind tunnel of width $1.0c$ and height $0.667c$ with the inboard surface of the wing being attached to the side wall of the tunnel without a peniche. The chord length c was 48 in (1.292 m). The reported chord Reynolds number of 4.6×10^6 was reduced to 4.35×10^6 as advised by Professor Bradshaw (personal communication). Transition was forced on both suction and pressure surfaces at 4% chord measured around the arc of the wing surface. A 7-hole pressure probe and hot-wires provided mean and turbulent velocities respectively.

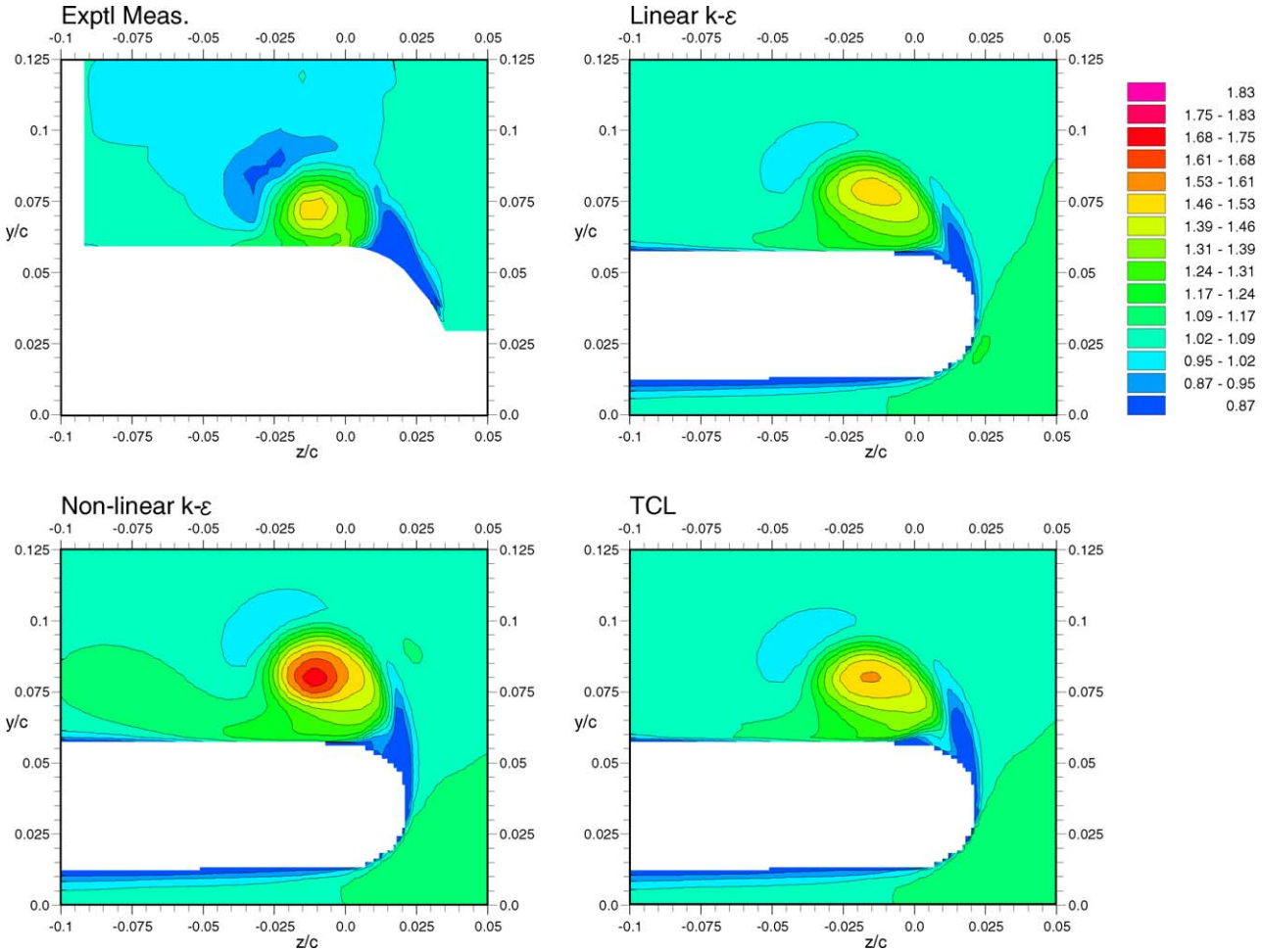

Fig. 4. Measured and computed contours of mean axial velocity at $x/c = -0.197$.

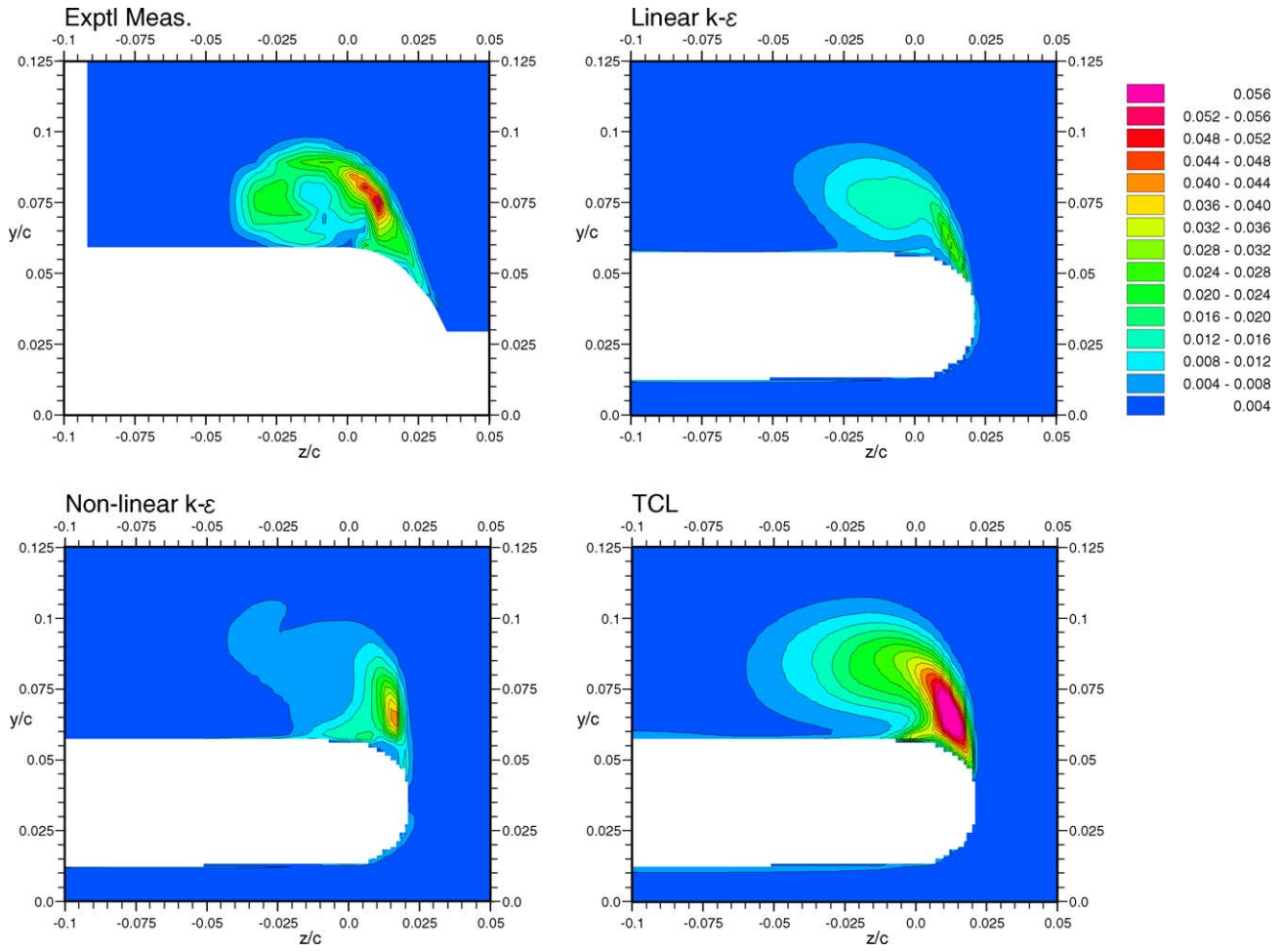

Fig. 5. Measured and computed contours of z-directed normal stress at $x/c = -0.197$.

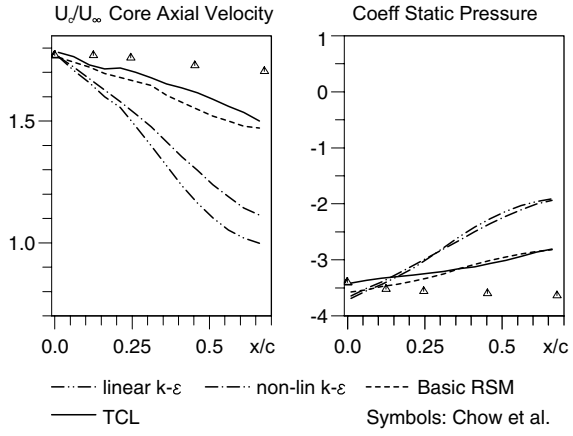

Fig. 6. Downstream variation of axial velocity and static pressure coefficient at the vortex centre.

The flow over the wing and near-field development of the vortex have been computed with STREAM (Lien and Leschziner, 1994). This is a fully 3D, elliptic finite-volume solver based on general curvilinear coordinates using the Rhie and Chow (1983) smoothing algorithm and employing the SIMPLE pressure-correction scheme. Convection is handled via a 2nd-order TVD scheme, initially on all variables but, as tests showed negligible effects, later on just mean-flow variables (with turbulence variables, whose level is dominated by source-terms rather than convection, discretized via upwind differencing). Into this solver the turbulence models and wall functions noted above were incorporated. The block-structured grid was created with the commercial meshing code ICEM. Because of the relatively large wing relative to the wind-tunnel dimensions, the whole wind-tunnel was included in the grid. Initially, following Dacles-Mariani et al. (1995), the upstream boundary was placed at $x/c = -1.135$, where a uniform streamwise velocity, zero secondary velocities and a turbulence intensity of 2% were applied. Convergence difficulties suggested, however, that this was too close to the wing for the pressure field to be undisturbed by the proximity of the wing. Thus a succession of tests led to the upstream boundary finally being placed at $x/c = -1.738$ where it was established the wing had no effect on the flow. (The streamwise coordinate, x, has its origin at the trailing edge of the airfoil and the leading edge at $x/c = -1.0 \times \cos(10°)$.) The downstream boundary was placed at $x/c = +0.678$ where zero gradient outflow conditions were applied to all variables.

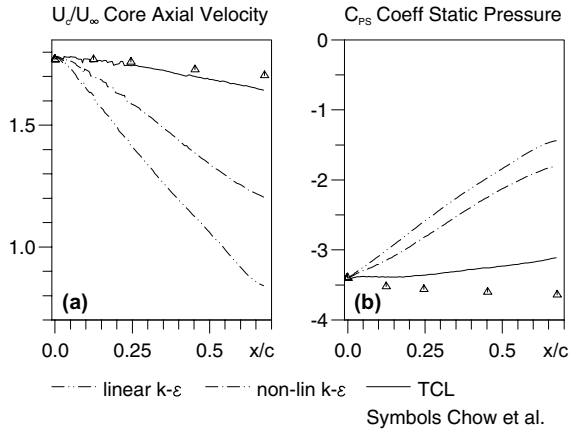

Fig. 7. Vortex centre axial velocity and static pressure coefficient development using the refined downstream grid.

Initial exploratory computations, reported by Craft et al. (2005), employed a grid comprising 2.2×10^6 nodes. The peak streamwise velocity attained in the eye of the vortex provided a highly sensitive indicator of under-resolution of the flow. The results obtained on that grid led to peak values of streamwise velocity in the vortex, just before the end of the wing, of 1.42 for the linear EVM and 1.63 for the TCL closure, compared with the measured peak of 1.77. Because the initial vortex formation is primarily an inviscid process it was felt unlikely that weaknesses in turbulence modelling could be principally the cause of this substantial disagreement. Computing resources were secured that enabled a grid refinement study. This exploration, Craft et al. (2005), using several grids, led to the conclusion that to achieve essentially grid-independent behaviour on the airfoil section approximately double the initial number of grid nodes were needed, an increase that had the effect of bringing the predicted peak velocity for both turbulence models into very close agreement, both with one another and with the data. Thus, for the 'whole-domain' computations reported here, 4.5 million cells in 26 blocks were adopted, corresponding to a maximum grid spacing of $5 \times 10^{-3}c$ as recommended in Dacles-Mariani et al. (1995) while, for cells adjacent to the airfoil, the height normal to the surface was around $1 \times 10^{-3}c$ which typically gave values of y^+ at the near-wall node in the range 40–100. A sample of the grid on the wing surface and wing-root wall is shown in Fig. 1. (For the single test with the low-Reynolds-number sublayer model 5.8 million nodes, the maximum available, were employed even though a somewhat coarser mesh was adopted outside the sublayer.)

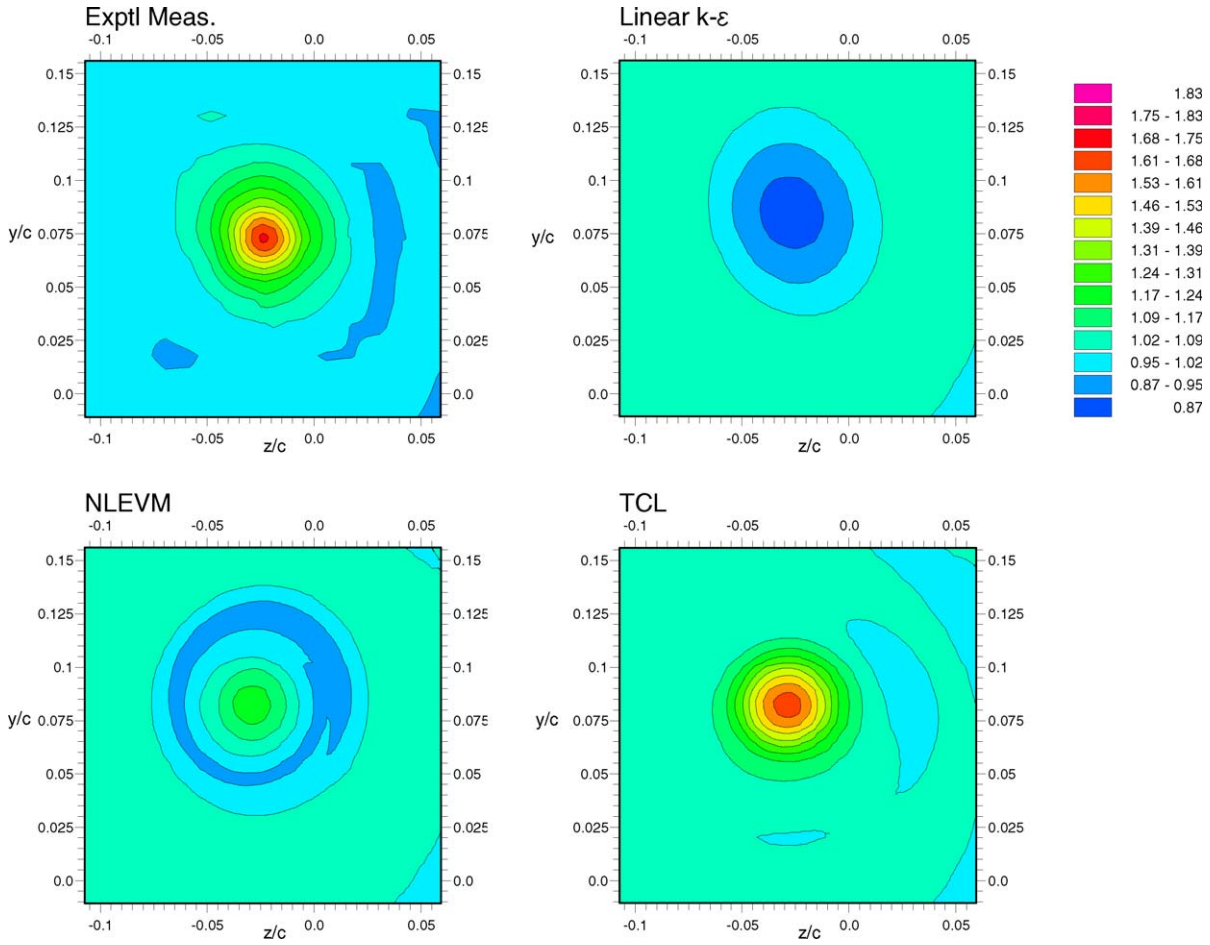

Fig. 8. Contours of cross-flow velocity, U/U_∞, at $x/c = 0.678$.

The block-structured grid caused grid refinements around the airfoil to be propagated downstream to regions where refinement was not needed, while leaving the downstream development of the vortex itself under-resolved. The final computations were thus performed in two stages. With uniform velocity prescribed at inlet with low turbulence levels, the first stage used the grid as described above (the results from which are documented in Figs. 3–6) to compute the flow on the airfoil and in the wake. The second stage limited attention to just the wake region, adopting an 18-block, purely Cartesian mesh of 4.8 million cells clustered around the vortex with an upstream boundary just downstream of the wing ($x/c = +0.001$). For all dependent variables the conditions applied at this inlet boundary were those interpolated from the best of the first-stage computations (with the TCL model). Taking the upstream and downstream grids together, there were then approximately 7.3×10^6 active cells in those calculations. The results thus obtained are those appearing in Fig. 7 and subsequent figures.

3. Consideration of the results

To give an overall impression of the flow field, Fig. 2 shows the streamlines near the wingtip and pressure contours computed with the TCL model. This shows clearly the shed streamwise vortex and the associated low pressure at the vortex core. To begin the quantitative comparisons, Fig. 3 compares the development of the measured mean velocity at the centre of the forming vortex with predicted results with four different models for the region over the wing itself. All models concur with the experiment to the extent that each calculation shows a rapid increase in maximum axial velocity at the vortex centre as the vortex proceeds to roll up as it is carried downstream along the airfoil. The maximum predicted value is in excess of $1.75U_\infty$ (and, for the non-linear EVM, greater than $1.8U_\infty$). However, while the linear EVM and the TCL second-moment closure track the reported experimental variation closely, both the "basic" second moment closure and the NLEVM show a significantly too early rise. With the basic second-moment closure the mismatch appears to have arisen from the "wall-reflection" terms in that model (see Appendices) having too great an influence near the outer edge of the wing where the wing surface is highly curved. Because the TCL model requires no such wall damping it is untroubled by the relatively complex surface topography. The non-linear EVM likewise requires no wall-reflection correction but, in this case, the problem has arisen from a too intense streamwise vortex having

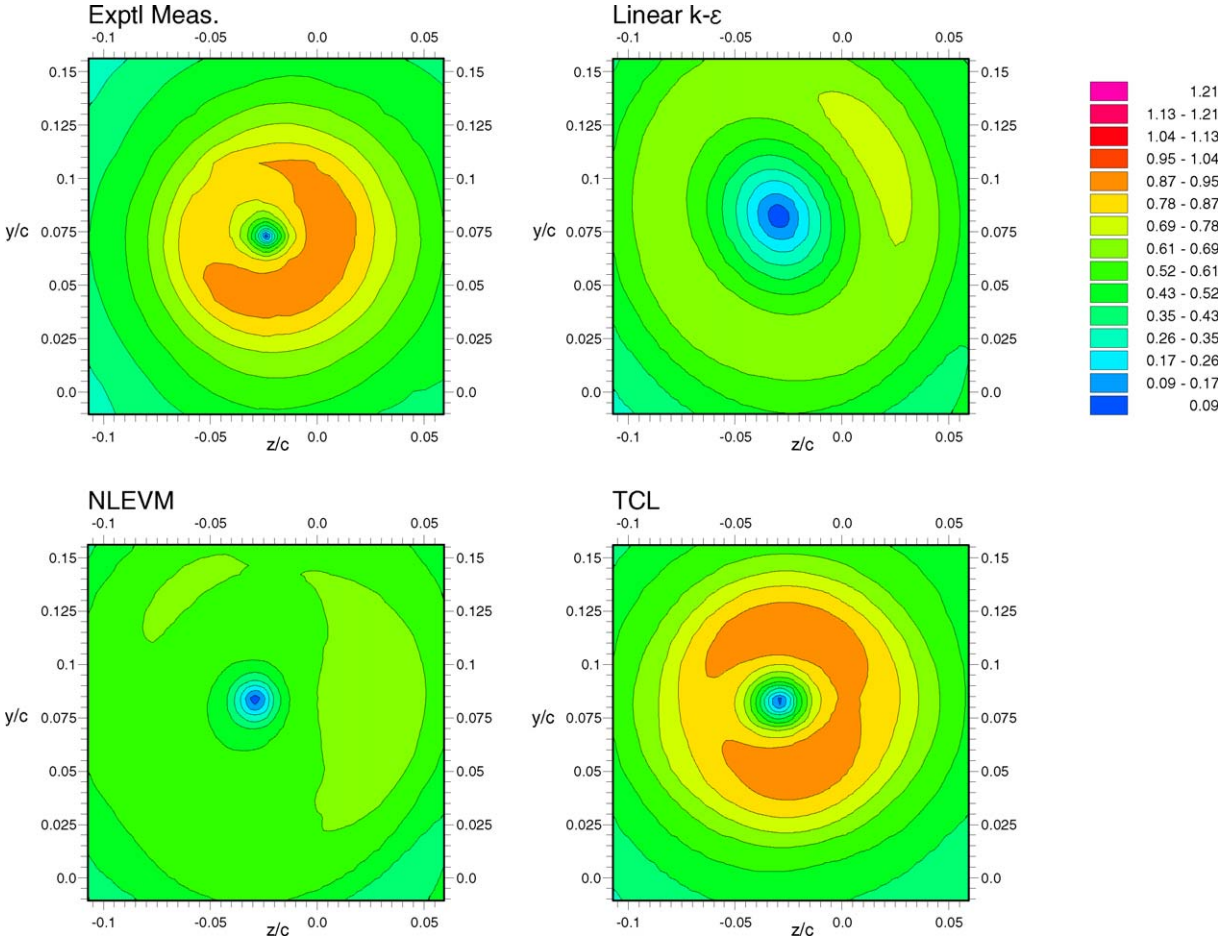

Fig. 9. Contours of cross-flow velocity, $(V^2 + W^2)^{1/2}/U_\infty$, at $x/c = 0.678$.

been created. Figs. 4 and 5 compare the measured and computed mapping of the axial velocity and the z-directed normal stress on the y–z plane in the vicinity of the vortex for $x/c = -0.197$ (i.e. towards the end of the wing). It is noted that, while the peak streamwise velocity is a little larger for the NLEVM computation, the difference is small compared with the large variations in Reynolds stress among the models, giving a practical demonstration of the fact that the initial vortex development is largely driven by inviscid effects.

Fig. 6 again shows the downstream variation of the maximum streamwise velocity at the vortex centre but this time the focus is on the region downstream of the airfoil's trailing edge. What is striking is that now there is a very great difference in the vortex evolution between the three different models. The experimental results show a slow decay of the axial velocity due partly to radial diffusion of streamwise momentum and partly to a slow rise of pressure at the vortex centre as the outer part of the vortex entrains fluid with zero angular momentum. Modelling that entrainment process is a challenge because in the stabilized inner core of the vortex (where the angular momentum increases with radius) turbulent stresses are damped by the streamline curvature while, at larger radii, mixing is amplified. The linear EVM exhibits a far too rapid decay with the centre velocity having reduced to the free stream value by $0.7c$ downstream. This errant behaviour is clearly associated with the well-known failure of eddy viscosity models to mimic the effects of streamline curvature. Of the two curvature-sensitive models, the non-linear EVM displays only modestly better behaviour than the linear EVM. This initially surprised us since it had been successful in modelling the swirling flow in a pipe (Craft et al., 1996b). However, on further reflection it was recognized that the model had also returned indifferent predictions of the swirling near wakes behind automobiles (Robinson, 2001; Suga et al., 2001). In contrast, the TCL closure displays less than half the decay of vortex-centre velocity as the NLEVM; that, however, is still considerably more than the experimental data.

As noted above, however, inspection of results showed that the block structured grid, designed to give dense coverage of the airfoil region, did not resolve adequately the downstream vortex. Thus, as described, the downstream wake was recomputed on a Cartesian mesh. These computations all employed as inlet conditions, immediately downstream of the airfoil's trailing edge, the interpolated data predicted by the 'whole domain' computation with the

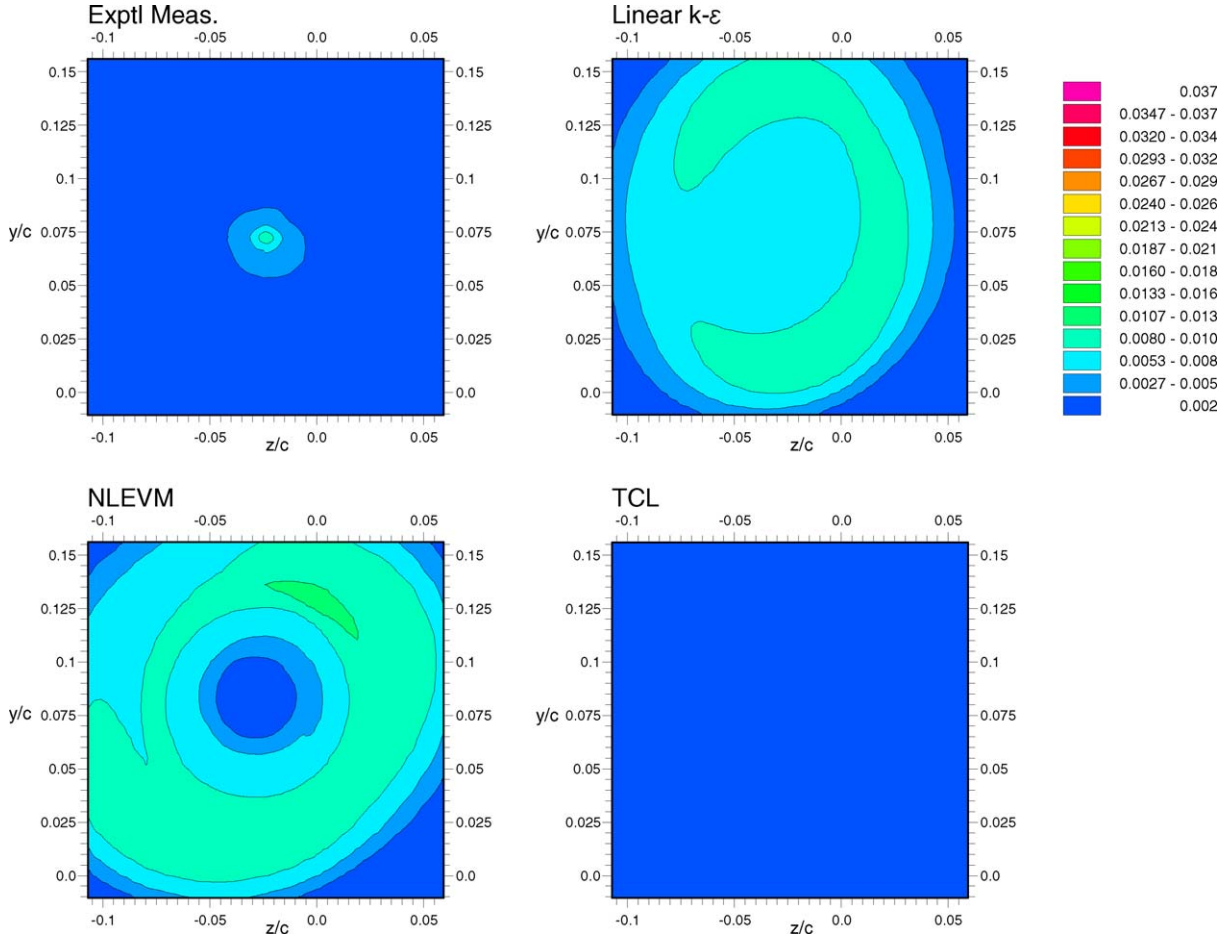

Fig. 10. Contours of axial normal stress, $\overline{u^2}/U_\infty^2$, at $x/c = 0.678$.

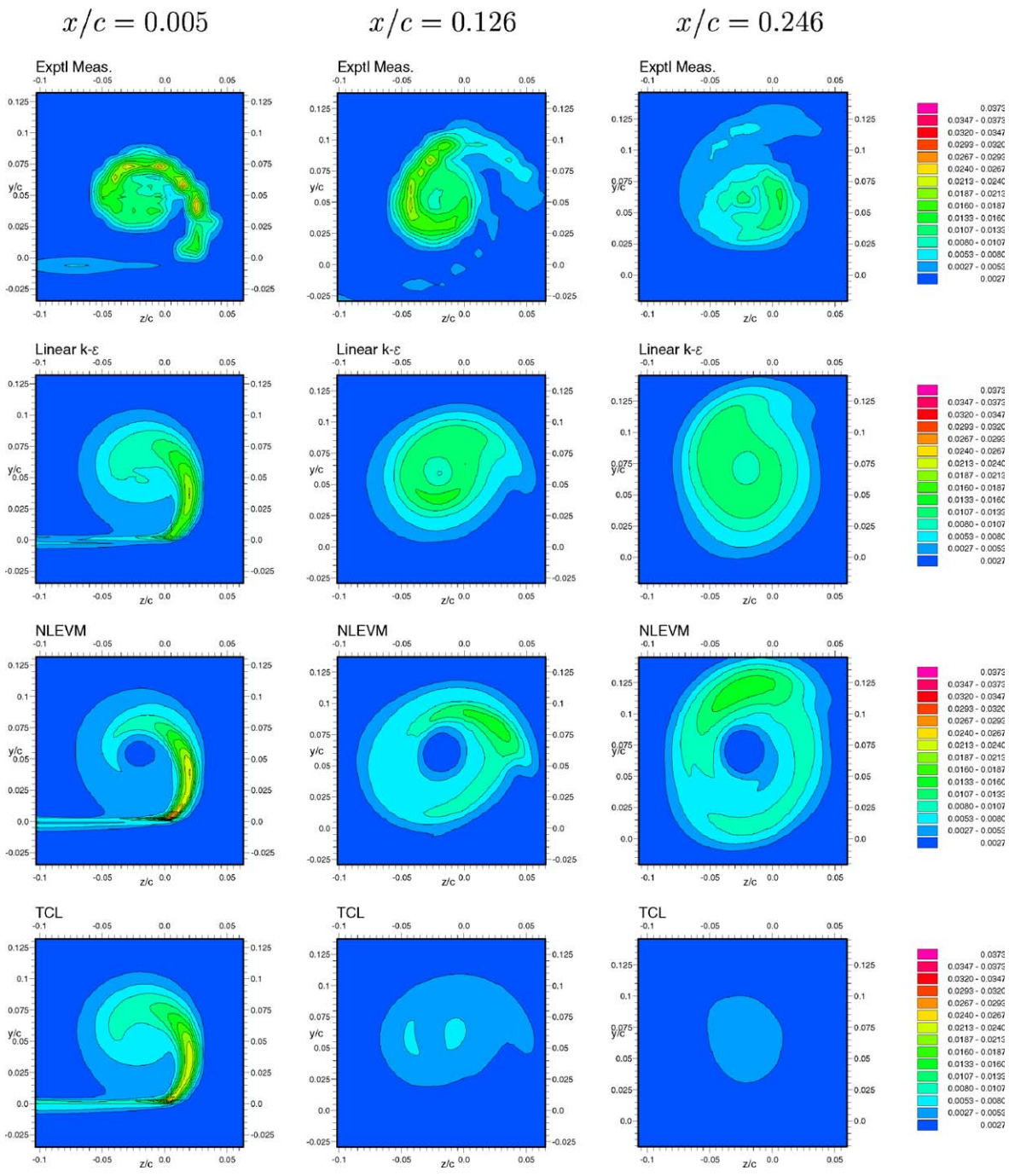

Fig. 11. Measured and computed development of the axial normal stress downstream of the wing.

TCL model as this provided the closest match to the experiment among the models examined. The consequent predicted development of the downstream vortex is summarized in Fig. 7a and b. While the relative variation of the vortex-centre velocity with the different models is the same as previously, there are some interesting differences. Firstly, the TCL model shows a noticeably slower decay with x so that, by the most downstream position for which data are available, the maximum velocity was $1.65U_\infty$ compared with $1.5U_\infty$ for the run shown in Fig. 6 and the measured value of $1.71U_\infty$. The NLEVM calculation also returned a slightly slower decay rate whereas the linear EVM actually shows a faster rate of decay with the result that by the downstream station the vortex-centre velocity is less than the free-stream value, that is, it has developed into a conventional wake. This behaviour is counter-intuitive, for one would expect that the reduction of false diffusion would diminish the rate of dilution. The reason a contrary response is shown is that, as may be inferred from Fig. 5, the Reynolds stress levels

used as the initial condition (obtained from the TCL 'whole domain' calculation) are a good deal higher than those returned at the same plane by the linear EVM 'whole domain' calculation. The variation of the static pressure at the centre of the vortex, shown in Fig. 7b, is broadly consistent with the velocity measurements.

A more complete picture of the vortex-jet/wake development for all three models is shown in the cross-sectional views. First let us compare the features of the different predictions with the measured behaviour as shown in Figs. 8–10, at the furthest station downstream, $x/c = 0.678$. The axial velocity, shown in Fig. 8, reveals striking differences among the models. As remarked above, for the linear EVM, the "jet" associated with the vortex has changed to a wake while the non-linear EVM exhibits a velocity peak within the vortex core but a wake beyond. In contrast, the TCL scheme exhibits a pattern that closely resembles the experimental data. A similar range of behaviour is found also in the magnitude of the cross-sectional plane velocity $(V^2 + W^2)^{1/2}$ shown in Fig. 9. While the linear EVM predicts a too rapid dispersal at all radii from the vortex centre, the non-linear model shows a much reduced dispersal rate in the inner core where the angular momentum of the vortex is increasing with radius but causes a much faster rate of radial diffusion beyond that core. Again the TCL model provides predictions that are in reasonable accord with the measured distribution of velocity at both small and large radii from the vortex centre.

The turbulent velocities likewise show striking differences, exemplified in Fig. 10 by the contours of axial normal stress $\overline{u^2}/U_\infty^2$. The linear and non-linear EVM display high residual levels of turbulence, with the non-linear model having a striking "hole" in the region of the vortex centre. In contrast, the TCL predictions show that turbulence levels have decayed below that registered by the contours (the maximum level being approximately 0.002). On first inspection, the experimental data appear to support this last result for the levels of the stress are much lower than predicted by the linear and non-linear EVMs and confined to a small zone coinciding closely with the region where the angular momentum is increasing. It was our initial conjecture that the low residual "turbulence" shown in the experiments was a spurious indicator caused by the precessing of the vortex. Such behaviour has been reported in other swirling flows in the literature, for example Morse (1980). However, such a convenient explanation is not supported by the data of the streamwise normal stress at stations further upstream. Fig. 11 shows, in miniature, the corresponding contours at three earlier stations downstream of the wing. Clearly, while just behind the wing the TCL predictions show a similar level to the experiments, the subsequent predicted rate of decay is far more rapid. It is relevant also to note the behaviour shown by the linear and non-linear EVM computations (recalling that these calculations all began with the TCL data as upstream boundary conditions immediately behind the wing). The linear EVM shows a considerably slower decay rate while the non-linear EVM is dominated by infidelities in the stress-deformation constitutive equation which immediately create a "hole" in the stresses in the vicinity of the vortex centre.

Despite the slower decay of the turbulent stresses with the linear EVM, the energy dissipation rate (not shown) decays less rapidly with this model than is predicted with the TCL scheme. While it is beyond the scope of the present paper to provide a firm explanation for the anomalous behaviour of the TCL model in this region of rapid change following the end of the wing, that is clearly an area where future research should be directed.

4. Conclusions

This study of the performance of three turbulence models in reproducing the near-field behaviour of the wing-tip vortex measured by Chow et al. (1997) has shown that:

- Linear eddy-viscosity models lead to a much too fast dispersal rate and should not be used for such flows.
- While the non-linear EVM of Suga (1995) leads to a diminution of mixing in the vortex core, its overall performance is scarcely better than the linear EVM. Further re-tuning of some of the empirical coefficients needs to be undertaken, perhaps by making them functions of the dimensionless vorticity:strain ratio.
- The TCL second-moment closure which, over the past decade, has been applied by the UMIST team to a wide range of complex flows near walls, returns, in many respects, close agreement with experiment in this complex free shear flow.
- Nevertheless, the initial decay of the turbulent stress field downstream of the wing is much faster with the TCL model than in the experiment. Further research is required to identify and remedy the cause of this anomaly.

Acknowledgements

The work reported has been undertaken as part of the M-DAW programme, supported by the European Commission through research grant G4RD-CT-2002-00837. Overall management of the programme has been provided by Mr. Alan Mann (Airbus-UK) and Dr. Eberhard Elsholz (Airbus-D). Computational resources provided by the University's Mason Centre for Environmental Flows are acknowledged. We are pleased to acknowledge the input provided by Professor P. Bradshaw and (through his thesis) Dr. J. Chow. Authors' names appear alphabetically.

Appendix A. The non-linear EVM of Suga (1995)

The model solves transport equations for k and ε of the form

Table A.1
Model coefficients in the non-linear stress–strain relation of Suga (1995)

c_1	c_2	c_3	c_4	c_5	c_6	c_7
−0.1	0.1	0.26	$-10c_\mu^2$	0	$-5c_\mu^2$	$5c_\mu^2$

$$\frac{\mathrm{D}k}{\mathrm{D}t} = P_k - \varepsilon + \frac{\partial}{\partial x_j}\left[(\nu + \nu_t/\sigma_k)\frac{\partial k}{\partial x_j}\right] \tag{A.1}$$

$$\frac{\mathrm{D}\varepsilon}{\mathrm{D}t} = c_{\varepsilon 1}\frac{\varepsilon P_k}{k} - c_{\varepsilon 2}\frac{\varepsilon^2}{k} + \frac{\partial}{\partial x_j}\left[(\nu + \nu_t/\sigma_\varepsilon)\frac{\partial \varepsilon}{\partial x_j}\right] \tag{A.2}$$

where $P_k = -\overline{u_i u_j}\partial U_i/\partial x_j$ and the coefficients are taken as $c_{\varepsilon 1} = 1.44$, $c_{\varepsilon 2} = 1.92$, $\sigma_\varepsilon = 1.3$.

The Reynolds stresses are modelled via the relation

$$\begin{aligned}\overline{u_i u_j} = {} & (2/3)k\delta_{ij} - \nu_t S_{ij} + c_1\frac{\nu_t k}{\varepsilon}(S_{ik}S_{kj} - (1/3)S_{kl}S_{kl}\delta_{ij}) \\ & + c_2\frac{\nu_t k}{\varepsilon}(\Omega_{ik}S_{kj} + \Omega_{jk}S_{ki}) + c_3\frac{\nu_t k}{\varepsilon}(\Omega_{ik}\Omega_{jk} - (1/3)\Omega_{lk}\Omega_{lk}\delta_{ij}) \\ & + c_4\frac{\nu_t k^2}{\varepsilon^2}(S_{ki}\Omega_{lj} + S_{kj}\Omega_{li})S_{kl} \\ & + c_5\frac{\nu_t k^2}{\varepsilon^2}(\Omega_{il}\Omega_{lm}S_{mj} + S_{il}\Omega_{lm}\Omega_{mj} - (2/3)S_{lm}\Omega_{mn}\Omega_{nl}\delta_{ij}) \\ & + c_6\frac{\nu_t k^2}{\varepsilon^2}S_{ij}S_{kl}S_{kl} + c_7\frac{\nu_t k^2}{\varepsilon^2}S_{ij}\Omega_{kl}\Omega_{kl}\end{aligned} \tag{A.3}$$

where

$$S_{ij} = \frac{\partial U_i}{\partial x_j} + \frac{\partial U_j}{\partial x_i}, \qquad \Omega_{ij} = \frac{\partial U_i}{\partial x_j} - \frac{\partial U_j}{\partial x_i} \tag{A.4}$$

The turbulent viscosity is defined as $\nu_t = c_\mu k^2/\varepsilon$ with

$$c_\mu = \frac{0.3}{1 + 0.35\eta^{3/2}}[1 - \exp(-0.36\exp(0.75\eta))] \tag{A.5}$$

where $\eta = \max(S, \Omega)$ and

$$S = \frac{k}{\varepsilon}\sqrt{0.5S_{ij}^2}, \qquad \Omega = \frac{k}{\varepsilon}\sqrt{0.5\Omega_{ij}^2} \tag{A.6}$$

The coefficients $c_1 \ldots c_6$ are given in Table A.1.

Appendix B. The basic stress-transport model

Transport equations are solved for $\overline{u_i u_j}$ of the form

$$\frac{\mathrm{D}\overline{u_i u_j}}{\mathrm{D}t} = P_{ij} + \phi_{ij} - \varepsilon_{ij} + d_{ij} \tag{B.1}$$

where the generation rate, P_{ij}, is given by

$$P_{ij} = -\overline{u_i u_k}\frac{\partial U_j}{\partial x_k} - \overline{u_j u_k}\frac{\partial U_i}{\partial x_k} \tag{B.2}$$

The pressure–strain, ϕ_{ij}, is modelled as

$$\begin{aligned}\phi_{ij} &= \phi_{ij1} + \phi_{ij2} + \phi_{ijw} \\ \phi_{ij1} &= -c_1\varepsilon a_{ij} \\ \phi_{ij2} &= -c_2(P_{ij} - (1/3)P_{kk}\delta_{ij}) \\ \phi_{ijw} &= c_1'(\varepsilon/k)(\overline{u_l u_m}n_l n_m\delta_{ij} - (3/2)\overline{u_i u_l}n_j n_l - (3/2)\overline{u_j u_l}n_i n_l)f_y \\ &\quad + c_2'(\phi_{lm2}n_l n_m\delta_{ij} - (3/2)\phi_{il2}n_j n_l - (3/2)\phi_{jl2}n_i n_l)f_y\end{aligned} \tag{B.3}$$

where $a_{ij} = \overline{u_i u_j}/k - (2/3)\delta_{ij}$; $\underline{n}$ is the wall-normal direction; $f_y = (k^{3/2}/\varepsilon)/(c_l y)$ where y is the wall distance, and the coefficients are taken as $c_1 = 1.8$, $c_2 = 0.6$, $c_1' = 0.5$, $c_2' = 0.3$ and $c_l = 2.55$.

The dissipation is taken as isotropic, so $\varepsilon_{ij} = (2/3)\varepsilon\delta_{ij}$, while the diffusion is modelled via a gradient-diffusion approximation as

$$d_{ij} = \frac{\partial}{\partial x_k}\left[\left(\nu\delta_{kl} + c_s\frac{k}{\varepsilon}\overline{u_k u_l}\right)\frac{\partial \overline{u_i u_j}}{\partial x_l}\right] \tag{B.4}$$

with coefficient $c_s = 0.22$.

The dissipation rate, ε, is obtained from its own modelled transport equation

$$\frac{\mathrm{D}\varepsilon}{\mathrm{D}t} = c_{\varepsilon 1}\frac{\varepsilon P_{kk}}{2k} - c_{\varepsilon 2}\frac{\varepsilon^2}{k} + \frac{\partial}{\partial x_k}\left[\left(\nu\delta_{lk} + c_\varepsilon\frac{k}{\varepsilon}\overline{u_k u_l}\right)\frac{\partial \varepsilon}{\partial x_l}\right] \tag{B.5}$$

with $c_{\varepsilon 1} = 1.44$, $c_{\varepsilon 2} = 1.92$ and $c_\varepsilon = 0.18$.

Appendix C. The TCL stress-transport model

In this case, the pressure–strain, ϕ_{ij}, is modelled as

$$\begin{aligned}\phi_{ij} = {} & -c_1\varepsilon[a_{ij} + c_1'(a_{ik}a_{jk} - (1/3)A_2\delta_{ij})] - f_A'\varepsilon a_{ij} \\ & - 0.6(P_{ij} - (1/3)\delta_{ij}P_{kk}) + 0.3a_{ij}P_{kk} \\ & - 0.2\left[\frac{\overline{u_k u_j}\,\overline{u_l u_i}}{k}\left[\frac{\partial U_k}{\partial x_l} + \frac{\partial U_l}{\partial x_k}\right] - \frac{\overline{u_l u_k}}{k}\left[\overline{u_i u_k}\frac{\partial U_j}{\partial x_l} + \overline{u_j u_k}\frac{\partial U_i}{\partial x_l}\right]\right] \\ & - c_2[A_2(P_{ij} - D_{ij}) + 3a_{mi}a_{nj}(P_{mn} - D_{mn})] \\ & + c_2'\left\{\left(\frac{7}{15} - \frac{A_2}{4}\right)(P_{ij} - (1/3)\delta_{ij}P_{kk}) \right. \\ & + 0.1\left[a_{ij} - \frac{1}{2}(a_{ik}a_{kj} - (1/3)\delta_{ij}A_2)\right]P_{kk} - 0.05a_{ij}a_{lk}P_{kl} \\ & + 0.1\left[\left(\frac{\overline{u_i u_m}}{k}P_{mj} + \frac{\overline{u_j u_m}}{k}P_{mi}\right) - (2/3)\delta_{ij}\frac{\overline{u_l u_m}}{k}P_{ml}\right] \\ & + 0.1\left[\frac{\overline{u_l u_i}\,\overline{u_k u_j}}{k^2} - (1/3)\delta_{ij}\frac{\overline{u_l u_m}\,\overline{u_k u_m}}{k^2}\right]\left[6D_{lk}\right. \\ & \left.\left. + 13k\left[\frac{\partial U_l}{\partial x_k} + \frac{\partial U_k}{\partial x_l}\right]\right] + 0.2\frac{\overline{u_l u_i}\,\overline{u_k u_j}}{k^2}(D_{lk} - P_{lk})\right\}\end{aligned} \tag{C.1}$$

where the stress anisotropy invariants are defined as

$$A_2 = a_{ij}a_{ij}, \quad A_3 = a_{ij}a_{jk}a_{ki}, \quad A = 1 - (9/8)(A_2 - A_3) \tag{C.2}$$

and the coefficients c_1, c_1', f_A', c_2 and c_2' are taken as

$$\begin{aligned}c_1 &= 3.1A_2^{1/2}A_f, \quad c_1' = 1.1, \quad f_A' = A \\ c_2 &= \min(0.55, 1.6/(1 + S)) \\ c_2' &= \min(0.6, A) + 2.5(S - \Omega)/(3 + S + \Omega) - 1.5S_I\end{aligned}$$

with

$$A_f = \begin{cases}(A/14)^{1/2} & A < 0.05 \\ A/0.7^{1/2} & 0.05 < A < 0.7 \\ A^{1/2} & A > 0.7\end{cases} \qquad S_I = S_{ij}S_{jk}S_{ki}/(S_{lm}S_{lm})^{3/2}$$

and S, Ω as given in Eq. (A.6).

The tensor D_{ij} implies

$$D_{ij} = -\overline{u_i u_k}\frac{\partial U_k}{\partial x_i} - \overline{u_j u_k}\frac{\partial U_k}{\partial x_i}$$

The dissipation is approximated by

$$\varepsilon_{ij} = (2/3)\varepsilon\delta_{ij}f_\varepsilon + \frac{\overline{u_i u_j}}{k}\varepsilon(1 - f_\varepsilon) \tag{C.3}$$

where $f_\varepsilon = A^{3/2}$, and diffusion is modelled as in Eq. (B.4).

The dissipation rate, ε, is obtained from a transport equation similar to Eq. (B.5), except that the coefficients $c_{\varepsilon 1}$ and $c_{\varepsilon 2}$ are taken as

$$c_{\varepsilon 1} = 1.0, \qquad c_{\varepsilon 2} = 1.92/(1 + 0.7A_2^{1/2}A)$$

References

Baldwin, B.S., Barth, T.J., 1990. A 1-equation turbulence model for high-Reynolds number wall-bounded flows. NASA TM 102847.

Batchelor, G.K., 1964. Axial flow in trailing line vortices. J. Fluid Mech. 20, 645–648.

Carlin, G., Dadone L., Spencer, R., 1989. Results of an experimental investigation of blade-tip vortex-modification devices. NASA Contractor Report CR-181853.

Chigier, N.A., Corsiglia, V.R., 1971. Tip vortices – velocity distributions. NASA TM X-62,087, NASA.

Chigier, N.A., Corsiglia, V.R., 1972. Wind-tunnel studies of wing-wake turbulence. J. Aircraft 9, 820–825.

Chow, J.S., 1994. Turbulence measurements in the near-wake of a wing-tip vortex. Thermosciences Division Rep. No. MD-69, Mechanical Engineering Department, Stanford University.

Chow, J.S., Zilliac, G., Bradshaw, P., 1997. Turbulence measurements in the near field of a wingtip vortex. NASA Tech Mem 110418, NASA.

Craft, T.J., Launder, B.E., 2001. Principles and performance of TCL-based second-moment closures. Flow, Turbulence Combust. 66, 355–372.

Craft, T.J., Ince, N.Z., Launder, B.E., 1996a. Recent developments in second-moment closure for buoyancy-affected flows. Dyn. Atmos. Oceans 25, 99–114.

Craft, T.J., Launder, B.E., Suga, K., 1996b. Development and application of a cubic eddy-viscosity model of turbulence. Int. J. Heat Fluid Flow 17, 108–115.

Craft, T.J., Gerasimov, A.V., Iacovides, H., Launder, B.E., 2002. Progress in the generalization of wall-function treatments. Int. J. Heat Fluid Flow 23, 148–160.

Craft, T.J., Launder, B.E., Robinson, C.M.E., 2005. The computational modelling of wing-tip vortices and their near-field decay. In: Rodi, W., Mulas, M. (Eds.), Engineering Turbulence Modelling and Measurement – 6. Elsevier, Amsterdam.

Dacles-Mariani, J., Zilliac, G., Chow, J.S., Bradshaw, P., 1995. Numerical/experimental study of a wingtip vortex in the near field. AIAA J. 33, 1561–1568.

De Jong, F.J., Govindan, T.R., Levy, R., Shamroth, S.J., 1988. Validation of a forward marching procedure to compute tip vortex generation processes for ship propeller blades. Scientific Research Associates Inc., Report R88-920023-F.

Gatski, T.W., Rumsey, C.L., 2002. Linear and non-linear eddy viscosity models. In: Launder, B., Sandham, N. (Eds.), Closure Strategies for Turbulent and Transitional Flows. Cambridge University Press, pp. 9–46.

Green, S.I., 1991. Correlating single-phase flow measurements with observations of vortex cavitation. J. Fluids Eng. 113, 125–129.

Green, S.I., Acosta, A.J., 1991. Unsteady flow in trailing vortices. J. Fluid Mech. 227, 107–134.

Heffernan, K.G., 1985. Trailing vortex attenuation devices. Ph.D. thesis, Naval Postgraduate School, Monterey.

Iacovides, H., Launder, B.E., Li, H-Y., 1996. Application of a reflection-free DSM to turbulent flow and heat transfer in a square-sectioned U-bend. Exp. Thermal Fluid Sci. 13, 419–429.

Launder, B.E., Li, S-P., 1994. On the elimination of wall-topography parameters from second-moment closure. Phys. Fluids 6, 999–1006.

Launder, B.E., Morse, A.P., 1979. Numerical prediction of axisymmetric free shear flows with a Reynolds stress closure. In: Durst, F. et al. (Eds.), Turbulent Shear Flows 1. Springer, Heidelberg, pp. 279–294.

Launder, B.E., Shima, N., 1989. A second moment closure for the near-wall sublayer: development and application. AIAA J. 27, 1319–1325.

Lee, H., Schetz, J.A., 1985. Experimental results for Reynolds number effects on trailing vortices. J. Aircraft 22, 158–160.

Lien, F-S., Leschziner, M.A., 1994. A general non-orthogonal finite-volume algorithm for turbulent flow at all speeds incorporating second-moment turbulence-transport closure. Comput. Meth. Appl. Mech. Eng. 114, 123–167.

Lumley, J.L., 1978. Computational modelling of turbulent flows. Adv. Appl. Mech. 18, 123–176.

Moore, D.W., Saffman, P.G., 1973. Axial flow in laminar trailing vortices. Proc. Roy. Soc. 333, 491–508.

Morse, A.P., 1980. ''Axisymmetric free shear flows with and without swirl'', Ph.D. thesis, University of London.

Rhie, C.M., Chow, W.L., 1983. Numerical study of the turbulent flow past an airfoil with trailing edge separation. AIAA J. 21, 1525–1532.

Robinson, C.M.E., 2001. Advanced CFD modelling of road-vehicle aerodynamics. Ph.D. thesis, UMIST.

Sotiropoulos, F., Patel, V.C., 1995. Application of Reynolds-stress transport models to stern and wake flows. J. Ship Res. 39, 263–283.

Srinivasan, G.R., McCroskey, W.J., Baeder, J.D., Edwards, T.A., 1988. Numerical simulation of tip vortices of wings in subsonic and transonic flows. AIAA J. 26, 1153–1162.

Suga, K., 1995. Development and application of a non-linear eddy viscosity model sensitized to stress and strain invariants. Ph.D. thesis, Faculty of Technology, University of Manchester.

Suga, K., Nagoaka, M., Horinouchi, N., Abe, K., Kondo, Y., 2001. Application of a three equation cubic eddy-viscosity model to 3-D turbulent flows by the unstructured grid method. Int. J. Heat Fluid Flow 22, 259–271.

Wolfshtein, M., 1969. The velocity and temperature distribution in one-dimensional flow with turbulence augmentation and pressure gradient. Int. J. Heat Mass Transfer 12, 301–318.